Passive bias-free non-reciprocal metasurfaces based on thermally nonlinear quasi-bound states in the continuum

Michele Cotrufo [1,2], Andrea Cordaro [3,4,5], Dimitrios L. Sounas [6], Albert Polman[4] & Andrea Alù [1,7] ✉

Non-reciprocal devices—in which light is transmitted with different efficiencies along opposite directions—are key technologies for modern photonic applications, yet their compact and miniaturized implementation remains an open challenge. Among different avenues, nonlinearity-induced non-reciprocity has attracted significant attention due to the absence of external bias and the ease of integrability within conventional material platforms. So far, nonlinearity-induced non-reciprocity has been demonstrated only in guided platforms using high-quality-factor resonators. Here we demonstrate ultrathin optical metasurfaces with a large non-reciprocal response for free-space radiation based on silicon thermo-optic nonlinearities. Our metasurfaces combine an out-of-plane asymmetry—necessary to obtain non-reciprocity—with in-plane broken symmetry, which finely tunes the radiative linewidth of quasi-bound states in the continuum. Third-order thermo-optic nonlinearities, engaged by the quasi-bound state in the continuum, are shown to enable over 10 dB of non-reciprocal transmission and less than 3 dB of insertion loss, for impinging average intensities smaller than 3 kW cm^{-2}. Numerical calculations suggest that the build-up and relaxation times of the non-reciprocal response can approach sub-microsecond scales, only limited by thermal dissipation. The demonstrated devices merge the field of non-reciprocity with ultrathin metasurface technologies, offering an exciting functionality for signal processing and routing, communications and protection of high-power laser cavities.

Non-reciprocal electromagnetic devices transmit light asymmetrically along opposite directions, forming key components to achieve ultimate control over the flow of light. However, non-reciprocal transmission is difficult to achieve in conventional media: Lorentz reciprocity[1] dictates that in any system with permittivity and permeability tensors that are symmetric, time invariant and linear, the transmission between a source and a detector is invariant if these are swapped. Breaking reciprocity, thus, requires lifting at least one of these conditions. Standard

[1]Photonics Initiative, Advanced Science Research Center, City University of New York, New York, NY, USA. [2]The Institute of Optics, University of Rochester, Rochester, NY, USA. [3]Van der Waals-Zeeman Institute, Institute of Physics, University of Amsterdam, Amsterdam, The Netherlands. [4]Center for Nanophotonics, AMOLF, Amsterdam, The Netherlands. [5]John A. Paulson School of Engineering and Applied Sciences, Harvard University, Cambridge, MA, USA. [6]Department of Electrical and Computer Engineering, Wayne State University, Detroit, MI, USA. [7]Physics Program, Graduate Center of the City University of New York, New York, NY, USA. ✉e-mail: aalu@g.cuny.edu

approaches for light isolation involve applying a d.c. magnetic bias to magneto-optical materials, which makes the permittivity tensor asymmetric. More recently, non-reciprocity has been achieved with time-variant materials, where some material properties, such as the refractive index, are modulated in time[2–11]. Finally, reciprocity can be broken by exploiting electromagnetic nonlinearities[12–25]. This approach has recently received substantial attention, due to the absence of any external form of bias and the universal working principle, directly integrable in a variety of conventional photonic platforms[21]. When an electromagnetic resonator couples asymmetrically to two input/output ports, the same power injected from different ports gives rise to different intracavity field intensities. In linear systems, such internal asymmetry is not sufficient to break reciprocity, and the port-to-port transmission remains the same in both directions. However, if the resonator is filled with a nonlinear material with an intensity-dependent permittivity, different intracavity intensities create different permittivity profiles, enabling large asymmetries in the power flow for opposite directions[21]. Remarkably, this mechanism does not require any applied bias—in essence, it is the signal itself to self-bias the device—and it does not require any absorption, because the unwanted beam is reflected rather than being absorbed, as instead required in the case of magnetism-based isolators. Moreover, this mechanism is agnostic to the specific source of third-order nonlinearity, and it can be implemented, for example, by exploiting either optical Kerr nonlinearity or thermo-optic effects. Although general constraints based on passivity and time-reversal symmetry prevent these devices from working as conventional isolators under simultaneous two-port excitation[22], they constitute an appealing technology for applications such as the non-reciprocal routing of pulsed signals[20] and protection of high-power lasers. Indeed, due to its simplicity and general applicability, the nonlinearity-based route to non-reciprocity has been successfully demonstrated in various frameworks, such as integrated Si and InP microcavities operating in the near-infrared[16,20], microwave circuits[19] and atomic systems[23–25]. However, all the devices investigated so far involve integrated systems coupled to optical waveguides or transmission lines, because in these devices wave–matter interactions can be carefully controlled and enhanced, and the typically weak optical nonlinearities can be engaged in a controllable fashion. A few theoretical proposals[17,18,26–28] have suggested that these phenomena may be also translated to optical metasurfaces coupled to propagating free-space plane waves, which may be used to realize free-space fully passive flat non-reciprocal devices. However, the experimental demonstration of nonlinearity-induced non-reciprocity in optical metasurfaces has so far been elusive, mainly due to the weak nonlinearities of the involved materials, and the corresponding stringent requirements in terms of operating intensities and low material loss.

In this work, we experimentally demonstrate the emergence of strong nonlinearity-induced non-reciprocity in amorphous silicon metasurfaces coupled to free-space radiation in the near-infrared regime (Fig. 1a). To create an asymmetric coupling between the metasurface and plane waves propagating along the two normal directions, the out-of-plane symmetry of the device is broken by leaving a thin unpatterned layer, whose thickness can be controlled to maximize non-reciprocity[18] when combined with the third-order nonlinearities naturally occurring in silicon. A major challenge to enable large non-reciprocity in metasurfaces is the typically weak interactions of light with ultrathin devices, which—when combined with the poor nonlinearity of optical materials—results in negligible transmission asymmetries, and explains the lack of an experimental demonstration of these concepts to date. Here we address this issue by introducing tailored in-plane broken symmetries that carefully control a quasi-bound state in the continuum (q-BIC)[29]. In turn, the q-BIC linewidth tailors the metasurface resonant response, enhancing the nonlinear interactions with the incoming waves and hence minimizing the operating intensity, as well as simultaneously maintaining a large transmission contrast.

Based on these principles, we numerically and experimentally demonstrate a compact metasurface design that allows us to simultaneously and accurately control both the vertical asymmetry—necessary to obtain non-reciprocity—and the radiative linewidth of the targeted optical mode. These simple yet powerful design principles allow us to experimentally achieve transmission contrasts larger than 10 dB and insertion losses smaller than 3 dB for time-averaged impinging intensities smaller than 3 kW cm^{-2}, only limited by the material nonlinearity strength. Moreover, we experimentally demonstrate that the range of intensities over which non-reciprocity occurs can be fully controlled by the vertical asymmetry of the metasurface. In agreement with recent theoretical results[18], we also experimentally demonstrate a trade-off between the extent of input intensity range over which non-reciprocity occurs and the minimum insertion loss. Tailoring the metasurface geometry, we are able to operate close to the bounds allowed by this trade-off. We further investigate the source of third-order nonlinearity in our device by combining experimental measurements and numerical simulations. In our experimental settings, the nonlinear response appears to be dominated by thermo-optic effects, with rising and relaxation times of a few microseconds. We show how these characteristic times, which set the maximum operational speed of the device, could be reduced to a few hundreds of nanoseconds by engineering the thermal environment of the device, in agreement with recent experimental works[30–32].

Results

Before discussing our design and experiments, we emphasize an important aspect of non-reciprocal wave propagation. As elucidated recently[33], to assess the emergence of non-reciprocity in a two-port system, it is crucial to account for all the electromagnetic modes available at each port. Coupling to other modes may lead to phenomena like asymmetric mode conversion, which is very different, less practically relevant and easier to achieve than non-reciprocity[33]. In our scenario of a free-space periodic metasurface, the emergence of unwanted diffraction orders and/or polarization conversion may be responsible for additional modes, thus making it challenging to unequivocally observe non-reciprocal transmission. In our experiments, we address these issues by ensuring that the excitation/collection ports (defined below) support a single mode. We operate in a sub-wavelength regime where no diffraction orders can propagate, and no polarization conversion occurs due to the lack of material anisotropy and to the mirror symmetry of the unit cell with respect to the plane defined by the propagation direction and polarization (Supplementary Section 4).

Device design and numerical optimization

Figure 1a,b shows the geometry of our metasurface, consisting of a thin one-dimensional amorphous silicon grating placed on a glass-like substrate to allow mechanical handling. The metasurface is uniform along the y direction and periodic along the x direction with period a. The two single-mode excitation/collection ports (denoted as port 1 and port 2; Fig. 1a) correspond to plane waves propagating in opposite directions normal to the metasurface plane (z direction) with impinging electric field polarized along the direction of the nanowires forming the metasurface (y direction). Nonlinearity-induced non-reciprocity requires waves coming from the opposite ports to couple with different efficiencies to the same optical mode supported by the metasurface. In other words, the same intensity, injected from opposite directions, must result in different steady-state intracavity field intensities of the optical mode (Fig. 1b, inset). To induce and control such electromagnetic asymmetry, a residual silicon layer of thickness $t < H$ is left unpatterned, where H is the total thickness of the silicon layer. A device with $t = 0$ is symmetric along z (apart from the small asymmetry induced by the substrate), and thus, even in the presence of strong nonlinearities, it is expected to provide reciprocal wave transmission at any input power.
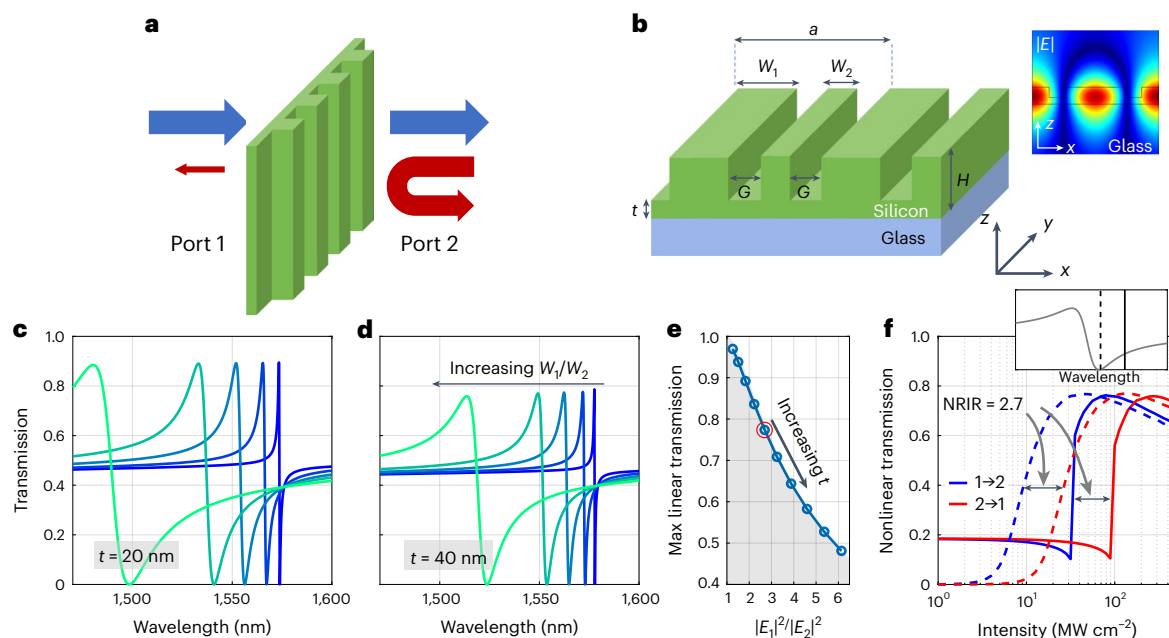
Fig. 1 | Passive free-space non-reciprocity using nonlinear metasurfaces with tailored asymmetries. a, Schematic of the non-reciprocal metasurface: by combining structural asymmetry and material nonlinearity, a wave impinging from either of the two sides of the device experiences markedly different transmission levels. **b**, Geometry and design parameters (additional details in the main text). The inset shows the field profile of the q-BIC excited by incoming plane waves. **c,d**, Calculated transmission spectra for a device with $t = 20$ nm (**c**) and $t = 40$ nm (**d**), fixed values of lattice constant ($a = 750$ nm), gaps ($G = 100$ nm) and total thickness ($H = 100$ nm), and different in-plane asymmetry values (W_1/W_2) ranging from 1.2 (dark blue lines) to 3.4 (light green lines). **e**, Scatter plot showing, for devices with a fixed value of $W_1/W_2 = 2.14$, the maximum linear transmission (vertical axis) and field asymmetry $E_1|^2/|E_2|^2$ (horizontal axis) for different values of t. The shaded area denotes the region allowed by equation (1). The red circle denotes the device considered in **f. f**, Calculated nonlinear transmission for the device marked by the red circle in **e**, for excitation from port 1 (blue lines) and port 2 (red lines), and for two excitation wavelengths, indicated by the solid and dashed lines in the top-right inset. The horizontal double-pointed arrows denote the extent of NRIR (2.7). For numerical convenience, in these simulations it is assumed that the nonlinear response is due to an instantaneous Kerr-like effect.

To enable strong nonlinearity-induced non-reciprocity, electromagnetic asymmetry is not sufficient, and strong nonlinear interactions are crucial. We maximize these phenomena by carefully controlling the radiative linewidth of the targeted resonant mode. Indeed, on one hand, it is desirable to reduce the radiative linewidth and hence maximize the quality factor (Q-factor) of the metasurface to strengthen the nonlinear interactions and minimize the required intensity to trigger these nonlinear phenomena[21]; on the other hand, to observe a large transmission contrast, the resonance linewidth must be larger than the linewidth of the impinging laser, which is particularly important when using pico- or femtosecond pulsed lasers. Too narrow-band responses also typically imply very selective angular responses, which hinder the possibility of focusing light on the sample to enhance the input intensity. In our device, we address these trade-offs by precisely controlling the Q-factor and frequency response of the metasurface through q-BIC engineering[29]. Such q-BICs have been proven to be a very useful platform to boost the Q-factor of metasurfaces and enhance nonlinear phenomena, such as lasing and second-harmonic generation[34–38]. Here we show that q-BICs, combined with nonlinear responses, can be used to dramatically enhance non-reciprocal wave transmission, by enhancing the metasurface Q-factor and simultaneously maintaining a large contrast in the Fano-like transmission spectra lineshape. We consider a unit cell composed of two silicon wires of lateral widths W_1 and W_2, separated by even gaps of width G (Fig. 1b). When the unit cell is symmetric ($W_1 = W_2$), the metasurface supports a localized mode that does not couple to free-space radiation due to symmetry, realizing a symmetry-protected BIC. Breaking the in-plane symmetry of the unit cell ($W_1 \neq W_2$) turns the BIC into a q-BIC with a finite radiative decay rate. This leads to the appearance of a Fano profile in the transmission spectrum, whose linewidth is carefully controlled by unit-cell asymmetry.

Figure 1c,d shows the numerically calculated linear transmission spectra of devices with $a = 750$ nm, $H = 100$ nm and $G = 100$ nm and different values of in-plane asymmetry W_1/W_2 ranging from 1.2 to 3.4 (Fig. 1d, horizontal arrow), and for $t = 20$ nm (Fig. 1c) and $t = 40$ nm (Fig. 1d). These results confirm that the linewidth of the Fano resonance can be continuously tuned by controlling the value of W_1/W_2. Figure 1b (inset) shows the electric-field intensity profile induced in a representative device by a plane-wave excitation resonant with the Fano transmission minimum. To quantify the electromagnetic asymmetry, we define[18] the ratio $\kappa = |E_1|^2/|E_2|^2$ of field intensities $|E_i|^2$ ($i = 1, 2$) induced in the device when the same power is injected from either port 1 or port 2. Devices with larger κ feature larger electromagnetic asymmetries, thereby leading to larger non-reciprocity when nonlinearities kick in. A second important metric is the maximum linear transmission T_{max}, obtained at the peak of the Fano lineshape, which determines the forward transmission of the device. As shown in Fig. 1c,d, T_{max} is affected by the vertical asymmetry: devices with smaller asymmetries, that is, smaller values of t for given H (Fig. 1c), feature higher transmission peaks compared with devices with larger asymmetries (Fig. 1d). This trend is not accidental, but instead rooted in a fundamental bound imposed by time-reversal symmetry[18,39,40]: for any two-port lossless device supporting a single resonant mode, the maximum transmission is bounded by $T_{max} \leq 4\kappa/(\kappa^2 + 1)$, and $T_{max} = 1$ can be obtained only with symmetric devices, that is, $\kappa = 1$. The parameter space allowed by this bound is depicted by the shaded area in Fig. 1e, whereas the blue circles represent the [κ, T_{max}] coordinates of different simulated devices with fixed in-plane geometry and different values of residual thickness t ranging from 0 to 90 nm. The plot shown in Fig. 1e confirms that all these devices maximize the trade-off T_{max} versus κ, that is, they feature the largest admissible T_{max} for a given electromagnetic asymmetry.

To numerically confirm the non-reciprocal response, we initially assume that the dominant nonlinearity in silicon is an instantaneous Kerr-like effect, such that the silicon permittivity depends on the instantaneous value of the local electric-field intensity $|\mathbf{E}|^2$ as $\varepsilon_{Si} = \varepsilon_{Si,lin} + \chi^{(3)}|\mathbf{E}|^2$, where $\chi^{(3)} = 2.8 \times 10^{-18}$ m^2 V^{-2} (ref. 41). This assumption allows us to simulate and understand the nonlinear behaviour of metasurfaces with reduced computational cost. As discussed later, a different third-order nonlinearity—thermo-optic effects—plays a role in the dynamics of these devices, due to the high repetition rate of our input laser. We note, however, that owing to the generality of the mechanism investigated here, any third-order nonlinearity that provides a permittivity shift $\Delta\varepsilon_{Si} \propto |\mathbf{E}|^2$ will lead to the desired non-reciprocal effects once steady state is achieved, although with possibly different transients[42,43].

Consider, for instance, a metasurface with $t = 40$ nm, $W_1 = 375$ nm and $W_2 = 175$ nm (Fig. 1e, device marked by the red circle). Figure 1f shows the simulated intensity-dependent port-to-port transmission for excitation from port 1 (blue curves) and port 2 (red curves) for two different excitation wavelengths. When the system is excited by a monochromatic wave tuned to the transmission minima of the Fano lineshape (Fig. 1f (inset), dashed vertical line), for both impinging directions, the transmission is zero at low intensities and it smoothly increases for higher intensities (Fig. 1f, dashed blue and red curves). However, due to the asymmetric response, the transmission growth with intensity is different for opposite excitation directions, resulting in large non-reciprocal transmission within a range of input intensities. When the excitation wavelength is instead red-detuned from the minima of the linear transmission spectrum (Fig. 1f (inset), vertical solid line, and Fig. 1f, solid blue and red lines), sharper transitions between the low and high transmission values are observed due to bistability[21]. Since the two transmission curves are scaled versions of each other, we can define the non-reciprocal intensity range (NRIR)[18] as the ratio between the intensities I_1 and I_2, which—when injected from opposite directions—leads to the same level of transmission. For the device shown in Fig. 1f, NRIR ≈ 2.7. Evidently, NRIR is always equal to the linear electromagnetic asymmetry[18], that is, NRIR $= \kappa = |E_1|^2/|E_2|^2$, and thus it does not depend on the excitation wavelength, as confirmed by Fig. 1f. For any excitation wavelength and propagation direction, the maximum transmission level in the nonlinear scenario (Fig. 1f) is identical to the one obtained in the linear transmission spectra (Fig. 1d). In particular, the aforementioned trade-off between the maximum linear transmission and the electromagnetic asymmetry leads to a corresponding trade-off between the maximum nonlinear forward transmission and the NRIR, as given by[18]

$$T_{max}^{nonlinear} \leq \frac{4 \times NRIR}{NRIR^2 + 1}. \tag{1}$$

Thus, although a wider NRIR can be obtained by increasing the electromagnetic asymmetry of the metasurface (that is, by increasing t), this comes at the cost of reduced transmission, implying a larger insertion loss. It is important to emphasize that the bound in equation (1) is due to the fact that a minimum amount of reflection must necessarily occur in asymmetric passive single resonators, and that the sub-unity transmission implied by equation (1) is not caused by absorption losses, which are—in principle—not required in our approach to obtain non-reciprocity. In this work, we focus on the scenario in which plane waves impinge on the metasurface at normal incidence. However, this is not a fundamental limitation, and the same device can be used to obtain nonlinearity-induced non-reciprocity even for tilted excitation directions, as numerically shown in Supplementary Section 6.

Before discussing the experimental results, we emphasize the different roles played by vertical ($t > 0$) and in-plane ($W_1 \neq W_2$) asymmetries in our design. The vertical asymmetry is required to ensure that the coupling rates between the optical mode supported by the grating and plane waves propagating along the $+z$ and $−z$ directions are different;

this asymmetry, combined with the material nonlinearity, gives rise to the non-reciprocal behaviour. The value of t also controls the NRIR; following equation (1), it, therefore, determines the minimum insertion loss of the device. The in-plane asymmetry, instead, is used as a knob to finely tune the Q-factor of the metasurface and hence maximize the nonlinear interactions, but it is not fundamentally needed to achieve non-reciprocity.

Linear characterization

We fabricated several metasurfaces with geometrical parameters close to the one used in Fig. 1 (details on the fabrication process are provided in the Methods), and with different values of in-plane asymmetry W_1/W_2 and vertical asymmetry t. The lattice constant a was varied between 700 and 800 nm to obtain resonant modes in the 1,450–1,650 nm spectral window. Figure 2a shows a top view and false-coloured cross-sectional SEM micrographs of two representative devices. A custom-built setup (Fig. 2b shows the schematic and Methods and Supplementary Section 1 describe the details) was used to measure the linear and nonlinear responses of the devices. The linear transmission spectra were measured by illuminating the sample with a broadband light linearly polarized along the y direction, and acquiring the transmitted signal with a spectrometer. Figure 2c shows the transmission spectra of five different devices with $t/H = 0.60$ and different values of in-plane asymmetry W_1/W_2. In agreement with the simulations shown in Fig. 1c,d, each spectrum features a Fano profile whose linewidth grows as W_1/W_2 increases. Although in simulations (Fig. 1c,d), the maximum and minimum transmission do not depend on W_1/W_2, in the measured spectra, the transmission contrast is reduced as the linewidth gets smaller (Fig. 2c, blue curves). This is primarily due to unwanted loss and imperfections introduced by the fabrication process, as well as the finite angular and spectral resolutions of our setup. As explained above, the maximum transmission level T_{max} is also fundamentally limited by the value of vertical asymmetry t. By reducing the vertical asymmetry, that is, reducing t for fixed H, the maximum transmission T_{max} is expected to increase, as confirmed by the measured spectra shown in Fig. 2d ($t/H = 0.34$) and Fig. 2e ($t/H = 0.16$).

Demonstration of nonlinearity-induced non-reciprocity

To experimentally demonstrate strong nonlinearity-induced non-reciprocal transmission through our metasurfaces, we measured the intensity-dependent transmission of several devices along the two directions. Based on the linear characterization (Fig. 2c–e), we selected devices with intermediate values of Q-factors, corresponding to linewidths (measured as the distance between the minimum and maximum of the Fano profile) ranging between 5 and 10 nm. For these devices, the minimum transmission level (determined by intrinsic loss and the resolution of our setup, as explained above) ranges between 5% and 15%. In our setup (Methods and Supplementary Section 1), a pulsed laser linearly polarized along the nanowires was weakly focused on the device under test. We first acquired the intensity-dependent transmission along one direction by sequentially sweeping the impinging power up and down, and then we flipped the sample to measure the transmission along the opposite direction. In doing so, particular care was taken to make sure that in both measurements, the excitation beam impinged on the sample at normal incidence (to avoid spurious shifts in the transmission spectra) and with the same spot size (to ensure that the intensity level was the same), and that the laser impinged at the same position within the metasurface (to minimize the impact of fabrication-induced inhomogeneities). Supplementary Section 2 outlines a more detailed description of this procedure.

Figure 3a–e shows the intensity-dependent transmission curves of five representative metasurfaces with vertical asymmetries ranging from large values ($t/H = 0.69$, Fig. 3a; $t/H = 0.61$, Fig. 3b) to intermediate values ($t/H = 0.50$, Fig. 3c; $t/H = 0.34$, Fig. 3d), and to a nominally symmetric device ($t/H = 0$, Fig. 3e). In each panel here, the left plot
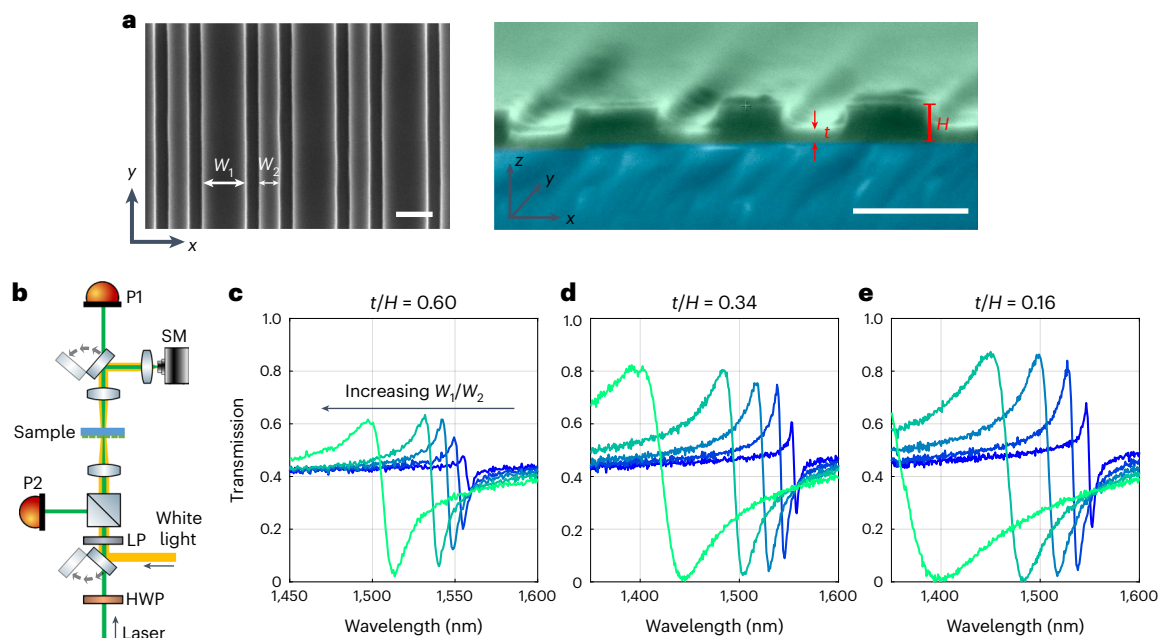
Fig. 2 | Fabrication and linear characterizations of metasurfaces.
a, Top-view (left) and false-coloured cross-sectional (right) SEM micrographs of the two fabricated metasurfaces. Scale bars, 300 nm. **b**, Schematic of the experimental setup used for linear and nonlinear measurements. HWP, half-wave plate; LP, linear polarizer; SM, spectrometer; P1 and P2, photodiodes. Methods and Supplementary Section 1 provide additional details. **c**–**e**, Measured normal-incidence transmission spectra of 15 different devices with a fixed lattice constant $a = 750$ nm, gap $G = 100$ nm and $H = 97$ nm. In each panel, the devices have the same residual thickness ($t = 58$ nm (**c**), $t = 33$ nm (**d**), $t = 16$ nm (**e**)), whereas different colours denote different in-plane asymmetries W_1/W_2, ranging from 1.2 to 3.4.
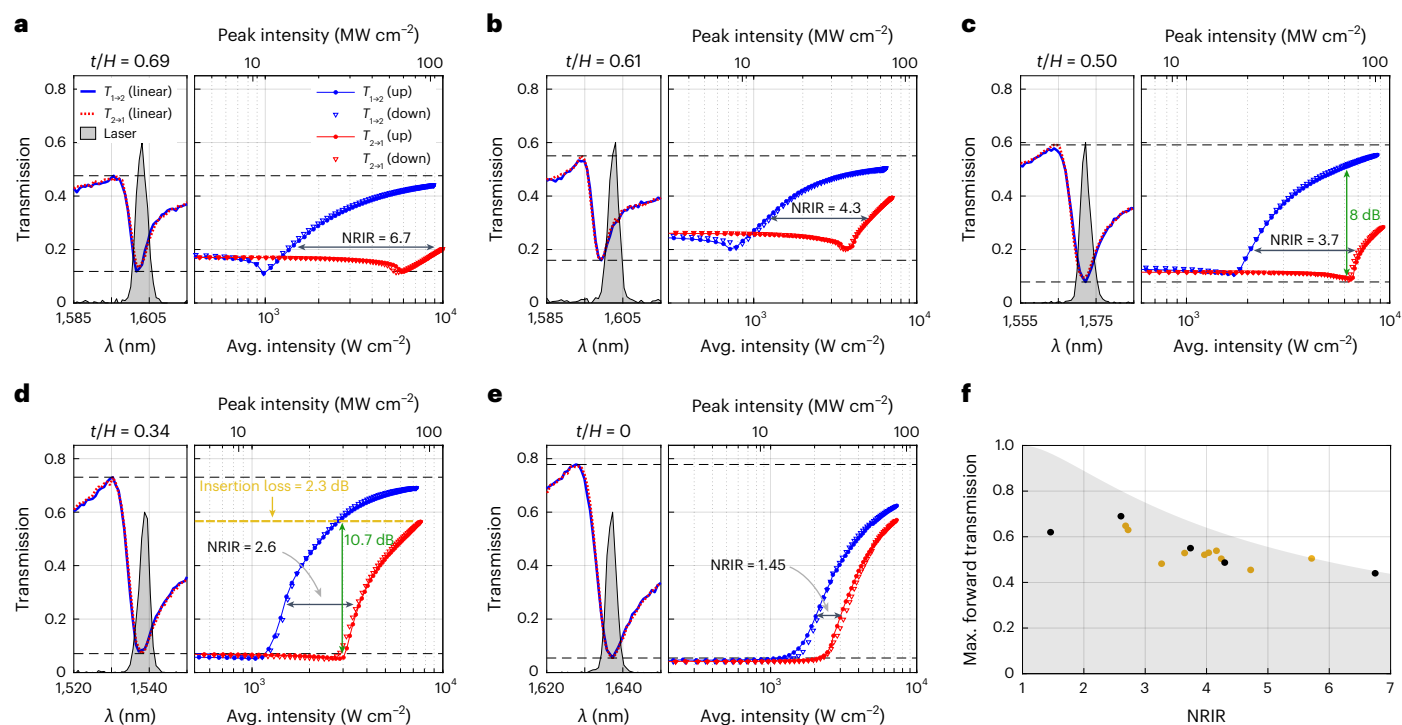

Fig. 3 | Experimental demonstration of nonlinearity-induced non-reciprocity. a–**e**, Linear and nonlinear characterizations of five devices with different values of t/H, as indicated by the text on top of each panel. In each panel, the left plot shows the laser spectrum (grey-shaded area) used in the nonlinear measurement, and the linear transmission spectra of the device measured along the two directions (solid blue and dashed red lines), acquired immediately before the corresponding nonlinear measurement. The right plot of each panel shows the measured nonlinear transmission versus impinging average intensity (lower axis) and peak intensity (upper axis), for a wave impinging from port 1 (blue symbols) and port 2 (red symbols), as well as for increasing and decreasing intensities. **f**, Scatter plot showing the NRIR and the maximum forward transmission of the devices in **a**–**e** (black dots), and several other measured devices (yellow dots). The grey-shaded area shows the trade-off corresponding to equation (1).

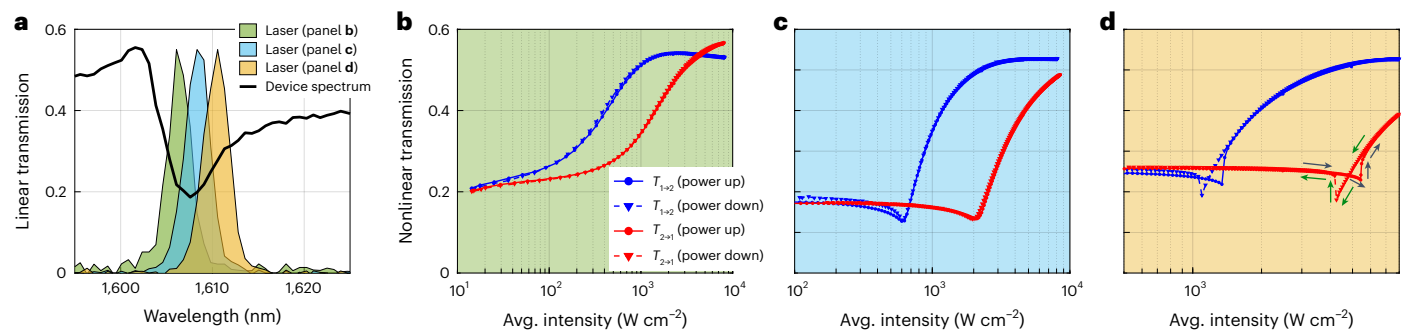**Fig. 4 | Non-reciprocal response of the same device for different excitation wavelengths. a**, Linear transmission spectra of the device under study (solid black lines), and three different excitation laser spectra (shaded areas, as shown in the legend). **b**–**d**, Non-reciprocal response of the metasurface for the three different excitation wavelengths shown in **a**, as the intensity is swept up and down. The blue (red) symbols denote transmission under excitation from port 1 (2). The arrows in **d** denote the portions of the curve where the input intensity is increasing (black arrows) or decreasing (green arrows).

shows the linear transmission spectra of the corresponding device, measured in the two directions (solid blue and dashed red lines) along with the spectrum of the laser (grey-shaded area) used in the corresponding nonlinear measurements. The right plot of each panel shows the corresponding nonlinear measurements, that is, the metasurface transmission for a fixed input laser wavelength, when exciting from port 1 (blue symbols) and port 2 (red symbols), versus the average input intensity (bottom horizontal axis) and peak input intensity (top horizontal axis). For each experimental run, we acquired the transmission as the power is swept up (circles joined by solid lines) and down (triangles). The good agreement between the nonlinear transmission curves recorded for increasing and decreasing power levels confirms that the observed changes in transmission are indeed due to a reversible intensity-dependent shift in the permittivity, and not to any irreversible damage to the device. For all these devices, we observed a clear non-reciprocal response for typical values of average intensities ranging between 1 and 5 kW cm^{-2}. As expected, the device with the largest vertical asymmetry ($t/H = 0.69$, Fig. 3a) also features the widest NRIR of 6.7, whereas its maximum transmission in the forward direction is limited to ~0.44. Importantly, the minimum and maximum transmission levels obtained in the nonlinear curves (Fig. 3a, horizontal dashed lines) match the minimum and maximum transmission levels observed in the corresponding linear transmission spectrum. When reducing the vertical asymmetry (Fig. 3b–d), the maximum forward transmission (blue symbols) increases, whereas the NRIR progressively shrinks. In the limit of a nominally symmetric device ($t = 0$, Fig. 3e), the range of intensities over which non-reciprocity can be observed is strongly reduced (NRIR ≈ 1.45). The small yet non-zero NRIR observed for $t = 0$ is due to a small residual electromagnetic asymmetry introduced by the glass substrate and by the tilted sidewalls of the grating, as confirmed by numerical simulations (Supplementary Section 3). Importantly, for all the devices considered in Fig. 3a–e, the transmission spectra measured along the two directions in the linear regime (that is, at very low powers) match exactly. This confirms that the devices are fully reciprocal in the linear regime and that the observed asymmetrical transmission verifies nonlinearity-induced non-reciprocity, and it is not due to other spurious effects such as mode conversion or polarization rotation.

The scatter plot in Fig. 3f shows the NRIR and the maximum forward transmission of the devices in Fig. 3a–e (black dots) and of several other measured devices (yellow dots), experimentally confirming the trade-off dictated by equation (1), which is highlighted by the grey-shaded area in Fig. 3f. As mentioned above, this fundamental trade-off, induced by time-reversal symmetry[18], requires that a certain level of reflection is always present in single-mode asymmetric structures, which, in turn, limits the maximum forward transmission. The fact that our devices lie very close to the edge of the trade-off curve (Fig. 3f)

indicates that the maximum forward transmission is only limited by a small intrinsic loss, and that most of the measured insertion loss is in fact due to the unavoidable back-reflection dictated by the bound in equation (1). Assuming realistic loss for amorphous silicon, we have numerically verified that less than 5% absorption is expected in our devices. Moreover, we note that for some of the devices shown in Fig. 3a–e, the maximum input power available in our experiment limits the achievable forward transmission, and thus, some of the points in Fig. 3f are actually closer to the boundary of the trade-off region. Remarkably, our devices can achieve large non-reciprocal contrasts (defined as the ratio between transmissions in the two directions for the same input intensity), and simultaneously provide a low insertion loss. Specifically, for intermediate values of NRIR, such as the device shown in Fig. 3d (NRIR = 2.6), a non-reciprocal ratio larger than 10 dB (Fig. 3d, green vertical line) is obtained for average intensities of about 3 kW cm^{-2} (corresponding to peak intensities of about 35 MW cm^{-2}), accompanied by an insertion loss of 2.3 dB. Importantly, this value of insertion loss is close to the minimum value imposed by the fundamental trade-off in equation (1) (Fig. 3f, shaded area), which affects any single-resonator device. As discussed by recent theoretical works, this fundamental limitation may be lifted by considering multiresonator metasurfaces[26,27]. In fact, in our devices, the non-reciprocal contrasts are mainly limited by the minimum transmission level, which sets the transmission along the backward direction within the NRIR. As discussed above, in realistic devices the minima of the Fano lineshape remain above zero due to fabrication imperfections and spectral averaging induced by finite spectral and angular linewidths of our excitation/collection system. Improvement in these factors may, therefore, lead to a substantial increase in the observed non-reciprocal transmission ratio.

Impact of spectral detuning on non-reciprocity
In all the measurements shown in Fig. 3, the excitation wavelength was kept close to the transmission minimum of the corresponding low-power spectrum. This small detuning helps in reducing the intensity required to observe a sizable change in transmission, but it also leads to a relatively smooth dependence of transmission on the input intensity. However, as also suggested by the calculation shown in Fig. 1f, the same device can give rise to different intensity-dependent transmission curves when the detuning between the impinging laser and Fano transmission minima is varied. Indeed, in Fig. 4, we report several measurements on the same device (whose linear transmission spectrum is shown in Fig. 4a, black curve) employing three different excitation laser spectra, as shown by the three shaded areas in Fig. 4a. For each excitation wavelength, we measured the nonlinear transmission in the two directions (Fig. 4b–d). All these measurements show a clear non-reciprocal response, but with markedly different lineshapes: when the excitation laser is tuned very close to the steep
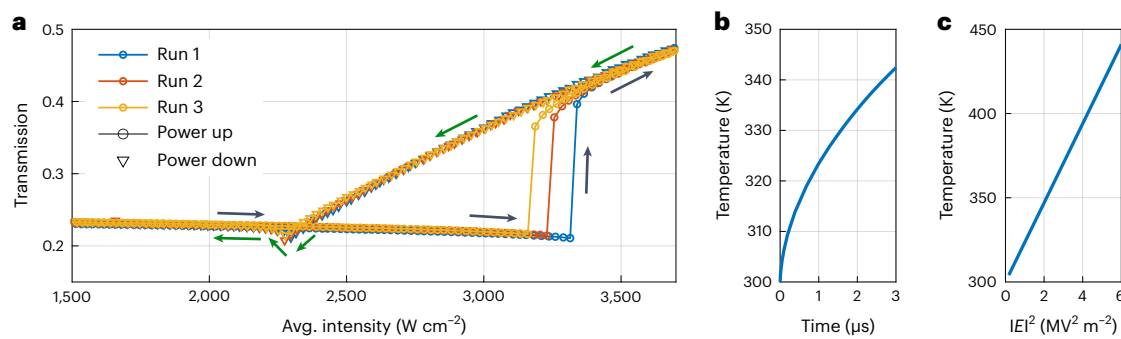
Fig. 5 | Bistability and impact of thermo-optic effects. a, Experimentally measured bistability response. We measured the forward transmission of the metasurface by scanning the power up and down three times. Different colours identify the three power ramps (see the legend). Increasing (decreasing) powers are denoted by circles (downward triangles). **b**, Numerical simulations of the time-dependent temperature variation at the centre of the metasurface (corresponding to the point of highest field intensity in Fig. 1b (inset)) due

to electromagnetic absorption and heating, assuming a CW excitation with a spatial Gaussian spot and average intensity $I_{avg} = 3$ kW cm^{-2}. The silicon absorption coefficient is assumed to be $\kappa = 0.01$. **c**, Calculated temperature increase at the centre of the metasurface after 3 μs for different impinging intensities. The horizontal axis shows the corresponding local field intensity at the centre of the metasurface.

edge of the Fano lineshape (Fig. 4a, green laser spectrum), a very smooth variation in the transmission curves is obtained at low intensities (Fig. 4b). As the excitation laser is progressively red-detuned (Fig. 4a, blue and yellow laser spectra), much sharper jumps occur in the intensity-dependent transmission curves (Fig. 4c,d), although at higher intensities. Such a behaviour can be useful to enhance the non-reciprocal transmission ratio at the desired intensities, by aligning the transmission minima in the backward direction with the transmission maxima in the forward direction.

Bistability and impact of thermo-optic effects

At large detunings (Fig. 4d), the intensity-dependent transmission curves show a clear hysteresis behaviour, where the values of transmission depend on whether the input intensity is increased or decreased (Fig. 4d, black and green arrows). This phenomenon is expected in systems with third-order nonlinearities, and it is due to the existence of multiple stable steady states for the same input power. Figure 5a shows a set of measurements (from a different device) where the bistability region is wider and clearer. Here we focus on the scenario in which the metasurface is excited from port 1; to verify the reproducibility of the bistability region, we repeated the up-and-down power ramp three times. For increasing intensities, the transmission experiences a sudden jump at impinging intensities between 3 and 3.5 kW cm^{-2}, corresponding to the transition from the first stable state to the second one. As the peak intensity is later decreased, the system remains in the second stable state until the intensity is about 2.25 kW cm^{-2}, after which it jumps back to the first stable state.

The presence of a clear bistable regime provides an important hint to shed light on the origin of nonlinearity at play in these experiments, particularly on its characteristic timescale. To showcase bistability, a nonlinear optical resonator must be able to retain some memory of the previous history of its internal state. In resonators with instantaneous nonlinearities (that is, where the intensity-dependent permittivity shift builds up and decays over times much shorter than any other relevant timescale), bistability can be observed when the power of a continuous-wave (CW) excitation is slowly swept up and down, while maintaining the excitation uninterrupted. This adiabatic variation in the external excitation allows the system to populate different stable states depending on its previous state. In our experiment, although the time-averaged impinging intensity is slowly swept up and down (on timescales of tens of seconds), the instantaneous impinging intensity is quickly and repeatedly turned on and off due to the pulsed excitation, composed of short pulses of a duration of ~2 ps separated by 12.5 ns. Thus, any nonlinearity with a characteristic build-up time faster than

a few nanoseconds would not lead to a bistable region with clearly separated branches in our experimental conditions. This observation suggests that slower nonlinear effects, such as thermo-optic effects, may have a significant role in the observed nonlinearity-induced non-reciprocal response.

To corroborate the impact of thermo-optic effects, we numerically calculated the time-dependent temperature increase in our devices under realistic experimental conditions and material parameters (Fig. 5b). For simplicity, and since we are only interested in estimating the electromagnetic-induced temperature increase, in these simulations we assume that the refractive index of silicon is not affected by the temperature variation. We simulated a finite metasurface with 200 periods illuminated by a CW beam with a Gaussian spot, and we calculated the time-dependent temperature increase at the metasurface centre. Supplementary Section 5 provides additional details of these calculations. For an impinging intensity of 3 kW cm^{-2} (similar to our experiments), the temperature at the centre of the metasurface quickly rises by more than 40 K within a time span of about 3 μs. Assuming a thermo-optic coefficient of $dn/dT = 2.3 \times 10^{-4}$ K^{-1} for amorphous silicon[44], this temperature shift will induce a relative spectral shift in the metasurface resonant frequency of $\Delta\omega/\omega \approx 10^{-3}$ to 10^{-2}, which is large enough to account for the transmission changes observed in our experiments. Thus, although fast nonlinearities (optical Kerr effect or carrier injection) may be playing a role in the observed non-reciprocity, our numerical simulations and the occurrence of a clear bistability region in the experimental data suggest that thermo-optic effects constitute the main nonlinearity at play in our experiments.

Although the nonlinear refractive-index change induced by thermo-optic effects depends on the absorption profile and subsequent thermal diffusion in a non-trivial way, in the thermal steady state the local change of refractive-index is still proportional to the local field intensity, thus leading to an effective third-order nonlinearity, namely, $\varepsilon_{Si} = \varepsilon_{Si,lin} + \chi_{eff}^{(3)}|\mathbf{E}|^2$. This is confirmed by the linear trend shown in Fig. 5c, where we plot—for different impinging intensities—the calculated temperature increase at the centre of the metasurface after 3 μs of illumination, as a function of the field intensity $|E|^2$ calculated at the same point. These simulated data, together with the thermo-optic coefficient for amorphous silicon[44], allow us to estimate an effective nonlinear permittivity of $\chi_{eff}^{(3)} \approx 10^{-14}$ m^2 V^{-2}, corresponding to an effective nonlinear refractive index of $n_{2,eff} \approx 10^{-10}$ cm^2 W^{-1}. These values are almost four orders of magnitude larger than the intrinsic nonlinear permittivity and nonlinear refractive index of crystalline silicon. Similar values of the effective nonlinear coefficients due to thermo-optic effects have been recently reported in the numerical calculations of

plasmonic waveguides[45]. Thus, in our experiment, thermo-optic effects give rise to an effective third-order nonlinearity, which—in the steady state—mimics the self-phase modulation of the Kerr effect, giving rise to strong non-reciprocal responses similar to those observed in waveguide-based devices[16,20]. On the other hand, we note that optical Kerr effects can also lead to cross-phase modulation, a phenomenon that can lead to protection against simultaneous back-propagating signals[46], and which cannot be mimicked by thermal effects. As a further caveat, we note that, even though at any given point inside the metasurface the local field intensity is proportional (in the steady state) to the local temperature increase, this proportionality factor varies across the unit cell due to the oscillations of the field intensity $|E|^2$ between the nodes and antinodes.

Due to the dynamic reciprocity limitations discussed above[22], this class of passive devices can be used as non-reciprocal routers only in scenarios where the delay between forward and backward excitation is long enough, such that the backward excitation does not experience the refractive-index change caused by the forward excitation. Thus, the build-up and relaxation times of the nonlinear response determines the minimum delay time between the forward and backward excitations. Although thermo-optic effects typically involve timescales longer than the optical Kerr effect, the simulations shown in Fig. 5b suggest that the build-up and relaxation times of the order of a few microseconds are possible in our device. Such short timescales are a consequence of the extremely small thickness of our metasurface. We further numerically verified (Supplementary Section 5) that by engineering the thermal environment and working with higher-intensity beams, the heating-up and cooling-down times can be brought to sub-microsecond timescales, for the same metasurface geometry. Moreover, sub-microsecond thermal dissipation timescales have been experimentally demonstrated in thin membranes and metasurfaces made of silicon[30–32] or other materials[47], which reported cooling-down times as short as 50 ns. Timescales in the range from 50 ns to 3 μs would enable non-reciprocal pulse routing when the back-reflected pulse has undergone round trips of lengths ranging from few tens to hundreds of metres, such as in light detection and ranging applications[20].

Finally, we discuss the potential presence of additional nonlinear effects and absorption. As mentioned above, the maximum transmission values obtained in nonlinear measurements are almost as high as those obtained in the corresponding linear measurements. For example, for the device shown in Fig. 3d, the maximum linear transmission is about 73%, whereas the maximum nonlinear transmission is 70%. This demonstrates that the nonlinear loss induced by two-photon absorption (TPA) is negligible in our experiments, in agreement with recent works that investigated the nonlinear performance of amorphous silicon[48]. We have also numerically verified these effects by repeating the simulations shown in Fig. 1f and including the TPA-induced loss. These calculations (Supplementary Section 7) confirm that for realistic values of TPA coefficients, the maximum transmission decreases by less than 5%, in good agreement with our experiments. Besides increasing the loss, TPA might also lead to free-carrier generation. However, we note that all our experimental data are consistent with the assumption that the frequency of the optical mode redshifts at high powers, and therefore that the permittivity increases. The injection of free carriers, on the other hand, is expected to decrease the permittivity[49], which would lead to a blueshift of the optical mode. We, therefore, conclude that, in our experimental conditions, free-carrier generation plays a negligible role. This is consistent with recent experimental studies that have found that the relaxation time of free carriers in amorphous silicon is much shorter than in crystalline silicon, with timescales shorter than 1 ps (refs. 50,51).

Conclusions and outlook

In this paper, we have experimentally demonstrated the occurrence of free-space fully passive and bias-free non-reciprocity in tailored silicon metasurfaces leveraging thermal nonlinearities enabled by q-BICs. By combining the third-order thermo-optic nonlinearities of silicon with out-of-plane symmetry breaking, we realized a metasurface for which the same input intensity beam, injected from opposite directions, leads to markedly different shifts in the refractive index, thereby enabling large non-reciprocal responses for free-space illumination. We emphasize that although these effects may be potentially observed in more conventional guided-mode resonances in gratings, the tailored q-BIC employed here leads to several critical advantages. By engineering the in-plane asymmetry of the metasurface, we have been able to accurately control the radiative linewidth of the metasurface and tailor the q-BIC, which allowed us to minimize the operating intensities and maintain a large transmission contrast. We experimentally demonstrated non-reciprocal transmission over a large range of intensities, with non-reciprocal ratios larger than 10 dB and insertion loss lower than 3 dB for average input intensities in the 1–5 kW cm^{-2} range. Remarkably, the level of forward transmission in our devices (up to 60% in Fig. 3d) is close to the typical values of 70%–90% obtained in commercial magneto-optical isolators (for example, Thorlabs, model IOT-4-1550-VLP), and it is dominated by reflections instead of material absorption, as instead happens in conventional isolators.

We further demonstrated that the non-reciprocal response can be largely tuned by simply controlling the thickness of a residual silicon layer, which makes our design particularly appealing for foundry-compatible fabrication. The values of insertion loss obtained in this work are close to the minimum value imposed by fundamental trade-offs, indicating that very little absorption occurs inside the metasurface. The insertion loss may be largely reduced by considering devices composed of two or more cascaded metasurfaces[26,27]. Moreover, we expect that further engineering of the unit-cell design, including tailored asymmetries and bianisotropy, could unlock additional functionalities such as three-port nonlinearity-induced circulators[52].

The powers required to obtain this non-reciprocal behaviour are set by the nonlinearity strength and by the Q-factor of the targeted optical mode. In particular, the required powers scale with the square of the Q-factor[21], and thus, we expect that even modest improvements to the fabrication process will drastically lower the operational intensities, bringing them closer to values achievable with standard optical-communication CW lasers.

In our experimental setting, the third-order nonlinear response is dominated by thermo-optic effects, whose typical timescales are much slower than the optical Kerr effect. Nonetheless, we demonstrated that, in our metasurface design, the build-up and relaxation time of the nonlinear response can be as short as a few hundreds of nanoseconds[30–32], mainly dependent on the thermal engineering of the environment surrounding the metasurface. We expect that by reducing the laser repetition rate and/or further increasing the thermal dissipation of the metasurface, the influence of thermo-optic effects can be strongly reduced, and much faster nonlinearities may become dominant. On the other hand, slow nonlinearities have recently attracted much attention, and they have been shown to unlock novel phenomena such as non-Markovian dynamics[43], limit cycles and chaos[53], as well as non-reciprocal pulse shaping and chaotic modulation[42].

Our approach and design principles can be readily adapted to different spectral ranges and materials. In the visible range, for example, where silicon is strongly absorptive, metasurfaces can be made out of strongly nonlinear chalcogenide glasses like As$_2$S$_3$ (ref. 54). Our results demonstrate a powerful and broadly applicable route to obtain magnet-free fully passive non-reciprocal propagation in free space, by leveraging q-BICs and material nonlinearities. This paves the way for several applications where small footprints, zero power consumption and ease of fabrication are needed, such as light detection and ranging systems, protection of high-power lasers and non-reciprocal signal routing for analogue computing. Moreover, although the devices demonstrated here require power levels that are too high for

applications in quantum information, the broad validity of this route to non-reciprocity allows the application of the same design principles to quantum metasurfaces, leading to non-reciprocal propagation at the few-photon power level[25].

Online content

Any methods, additional references, Nature Portfolio reporting summaries, source data, extended data, supplementary information, acknowledgements, peer review information; details of author contributions and competing interests; and statements of data and code availability are available at https://doi.org/10.1038/s41566-023-01333-7.

References

1. Collin, R. E. *Antennas and Radiowave Propagation* (McGraw-Hill, 1985).
2. Yu, Z. & Fan, S. Complete optical isolation created by indirect interband photonic transitions. *Nat. Photon.* **3**, 91–94 (2009).
3. Fang, K., Yu, Z. & Fan, S. Realizing effective magnetic field for photons by controlling the phase of dynamic modulation. *Nat. Photon.* **6**, 782–787 (2012).
4. Fang, K., Yu, Z. & Fan, S. Photonic Aharonov-Bohm effect based on dynamic modulation. *Phys. Rev. Lett.* **108**, 153901 (2012).
5. Lira, H., Yu, Z., Fan, S. & Lipson, M. Electrically driven nonreciprocity induced by interband photonic transition on a silicon chip. *Phys. Rev. Lett.* **109**, 033901 (2012).
6. Sounas, D. L., Caloz, C. & Alu, A. Giant non-reciprocity at the subwavelength scale using angular momentum-biased metamaterials. *Nat. Commun.* **4**, 2407 (2013).
7. Tzuang, L. D., Fang, K., Nussenzveig, P., Fan, S. & Lipson, M. Non-reciprocal phase shift induced by an effective magnetic flux for light. *Nat. Photon.* **8**, 701–705 (2014).
8. Estep, N. A., Sounas, D. L., Soric, J. & Alu, A. Magnetic-free non-reciprocity and isolation based on parametrically modulated coupled-resonator loops. *Nat. Phys.* **10**, 923–927 (2014).
9. Ruesink, F., Miri, M.-A., Alu, A. & Verhagen, E. Nonreciprocity and magnetic-free isolation based on optomechanical interactions. *Nat. Commun.* **7**, 13662 (2016).
10. Sohn, D. B., Kim, S. & Bahl, G. Time-reversal symmetry breaking with acoustic pumping of nanophotonic circuits. *Nat. Photon.* **12**, 91–97 (2018).
11. Sounas, D. L. & Alù, A. Non-reciprocal photonics based on time modulation. *Nat. Photon.* **11**, 774–783 (2017).
12. Fan, L. et al. An all-silicon passive optical diode. *Science* **335**, 447–450 (2011).
13. Bender, N. et al. Observation of asymmetric transport in structures with active nonlinearities. *Phys. Rev. Lett.* **110**, 234101 (2013).
14. Nazari, F. et al. Optical isolation via $\mathcal{PT}$-symmetric nonlinear Fano resonances. *Opt. Express* **22**, 9574–9584 (2014).
15. Mahmoud, A. M., Davoyan, A. R. & Engheta, N. All-passive nonreciprocal metastructure. *Nat. Commun.* **6**, 8359 (2015).
16. Yu, Y. et al. Nonreciprocal transmission in a nonlinear photonic-crystal Fano structure with broken symmetry. *Laser Photonics Rev.* **9**, 241–247 (2015).
17. Lawrence, M., Barton, D. R. & Dionne, J. A. Nonreciprocal flat optics with silicon metasurfaces. *Nano Lett.* **18**, 1104–1109 (2018).
18. Sounas, D. L. & Alù, A. Fundamental bounds on the operation of Fano nonlinear isolators. *Phys. Rev. B* **97**, 115431 (2018).
19. Sounas, D. L., Soric, J. & Alù, A. Broadband passive isolators based on coupled nonlinear resonances. *Nat. Electron.* **1**, 113–119 (2018).
20. Yang, K. Y. et al. Inverse-designed non-reciprocal pulse router for chip-based LiDAR. *Nat. Photon.* **14**, 369–374 (2020).
21. Cotrufo, M., Mann, S. A., Moussa, H. & Alu, A. Nonlinearity-induced nonreciprocity—Part I. *IEEE Trans. Microw. Theory Tech.* **69**, 3569–3583 (2021).
22. Shi, Y., Yu, Z. & Fan, S. Limitations of nonlinear optical isolators due to dynamic reciprocity. *Nat. Photon.* **9**, 388–392 (2015).
23. Müller, C., Combes, J., Hamann, A. R., Fedorov, A. & Stace, T. M. Nonreciprocal atomic scattering: a saturable, quantum Yagi-Uda antenna. *Phys. Rev. A* **96**, 053817 (2017).
24. Rosario Hamann, A. et al. Nonreciprocity realized with quantum nonlinearity. *Phys. Rev. Lett.* **121**, 123601 (2018).
25. Nefedkin, N., Cotrufo, M. & Alù, A. Nonreciprocal total cross section of quantum metasurfaces. *Nanophotonics* **12**, 589–606 (2023).
26. Jin, B. & Argyropoulos, C. Self-induced passive nonreciprocal transmission by nonlinear bifacial dielectric metasurfaces. *Phys. Rev. Appl.* **13**, 054056 (2020).
27. Mekawy, A., Sounas, D. L. & Alù, A. Free-space nonreciprocal transmission based on nonlinear coupled Fano metasurfaces. *Photonics* **8**, 139 (2021).
28. Solís, D. M. & Engheta, N. Nonreciprocal epsilon-near-zero-dielectric bilayers: enhancement of nonreciprocity from a nonlinear transparent conducting oxide thin film at epsilon-near-zero frequency. *Phys. Rev. Appl.* **17**, 034053 (2022).
29. Koshelev, K., Lepeshov, S., Liu, M., Bogdanov, A. & Kivshar, Y. Asymmetric metasurfaces with high-Q resonances governed by bound states in the continuum. *Phys. Rev. Lett.* **121**, 193903 (2018).
30. Vega-Flick, A. et al. Thermal transport in suspended silicon membranes measured by laser-induced transient gratings. *AIP Adv.* **6**, 121903 (2016).
31. Schmotz, M., Bookjans, P., Scheer, E. & Leiderer, P. Optical temperature measurements on thin freestanding silicon membranes. *Rev. Sci. Instrum.* **81**, 114903 (2010).
32. Ravichandran, N. K., Zhang, H. & Minnich, A. J. Spectrally resolved specular reflections of thermal phonons from atomically rough surfaces. *Phys. Rev. X* **8**, 041004 (2018).
33. Jalas, D. et al. What is—and what is not—an optical isolator. *Nat. Photon.* **7**, 579–582 (2013).
34. Kodigala, A. et al. Lasing action from photonic bound states in continuum. *Nature* **541**, 196–199 (2017).
35. Koshelev, K. et al. Nonlinear metasurfaces governed by bound states in the continuum. *ACS Photonics* **6**, 1639–1644 (2019).
36. Liu, Z. et al. High-Q quasibound states in the continuum for nonlinear metasurfaces. *Phys. Rev. Lett.* **123**, 253901 (2019).
37. Koshelev, K. et al. Subwavelength dielectric resonators for nonlinear nanophotonics. *Science* **367**, 288–292 (2020).
38. Hwang, M.-S. et al. Ultralow-threshold laser using super-bound states in the continuum. *Nat. Commun.* **12**, 4135 (2021).
39. Sounas, D. L. & Alu, A. Time-reversal symmetry bounds on the electromagnetic response of asymmetric structures. *Phys. Rev. Lett.* **118**, 154302 (2017).
40. Wang, K. X., Yu, Z., Sandhu, S. & Fan, S. Fundamental bounds on decay rates in asymmetric single-mode optical resonators. *Opt. Lett.* **38**, 100–102 (2013).
41. Boyd, R. W. *Nonlinear Optics* (Academic Press, 2020).
42. Hofstrand, A., Cotrufo, M. & Alù, A. Nonreciprocal pulse shaping and chaotic modulation with asymmetric noninstantaneous nonlinear resonators. *Phys. Rev. A* **104**, 053529 (2021).
43. Geng, Z. et al. Universal scaling in the dynamic hysteresis, and non-Markovian dynamics, of a tunable optical cavity. *Phys. Rev. Lett.* **124**, 153603 (2020).
44. Della Corte, F. G., Montefusco, M. E., Moretti, L., Rendina, I. & Rubino, A. Study of the thermo-optic effect in hydrogenated amorphous silicon and hydrogenated amorphous silicon carbide between 300 and 500 K at 1.55 μm. *Appl. Phys. Lett.* **79**, 168–170 (2001).
45. Khurgin, J. B., Sun, G., Chen, W. T., Tsai, W.-Y. & Tsai, D. P. Ultrafast thermal nonlinearity. *Sci. Rep.* **5**, 17899 (2015).

46. White, A. D. et al. Integrated passive nonlinear optical isolators. *Nat. Photon.* **17**, 143–149 (2023).

47. Abdollahramezani, S. et al. Electrically driven reprogrammable phase-change metasurface reaching 80% efficiency. *Nat. Commun.* **13**, 1696 (2022).

48. Matres, J. et al. High nonlinear figure-of-merit amorphous silicon waveguides. *Opt. Express* **21**, 3932–3940 (2013).

49. Lin, Q., Painter, O. J. & Agrawal, G. P. Nonlinear optical phenomena in silicon waveguides: modeling and applications. *Opt. Express* **15**, 16604–16644 (2007).

50. White, J., Cuzeau, S., Hulin, D. & Vanderhaghen, R. Subpicosecond hot carrier cooling in amorphous silicon. *J. Appl. Phys.* **84**, 4984–4991 (1998).

51. Haché, A. & Bourgeois, M. Ultrafast all-optical switching in a silicon-based photonic crystal. *Appl. Phys. Lett.* **77**, 4089–4091 (2000).

52. D'Aguanno, G., Sounas, D. L., Saied, H. M. & Alù, A. Nonlinearity-based circulator. *Appl. Phys. Lett.* **114**, 181102 (2019).

53. Peters, K. & Rodriguez, S. Limit cycles and chaos induced by a nonlinearity with memory. *Eur. Phys. J. Spec. Top.* **231**, 247–254 (2022).

54. Almeida, J., Barbano, E., Arnold, C. B., Misoguti, L. & Mendonça, C. R. Nonlinear optical waveguides in As_2S_3-Ag_2S chalcogenide glass thin films. *Opt. Mater. Express* **7**, 93–99 (2017).

Methods

Fabrication

The samples were fabricated with a standard top-down lithographic process. Glass coverslides ($25 \times 75 \times 1\ mm^3$, Fisher Scientific) were used as transparent substrates. The substrates were cleaned by placing them in an acetone bath inside an ultrasonic cleaner, and later in an oxygen-based cleaning plasma (PVA Tepla IoN 40). After cleaning, a layer of approximately 100 nm of amorphous silicon was deposited via a plasma-enhanced chemical vapour deposition process. A layer of electron-beam resist (ZEP 520-A) was then spin coated on top of the samples, and the desired pattern was written with an electron-beam tool (Elionix 50 keV). After ZEP development, the pattern was transferred to the underlying silicon layer via dry etching in an inductively coupled plasma machine (Oxford PlasmaPro System 100). Different copies of the same sample were fabricated in the same electron-beam lithography run, and then etched with different etching times to control the residual thickness t (Fig. 1). The resist mask was finally removed with a solvent (Remover PG). Supplementary Fig. 1a,b shows the false-coloured SEM images of the cross section of two fabricated devices, with different values of residual thicknesses t.

Optical characterization

The linear and nonlinear responses of the samples were measured with a custom-built setup (Fig. 2b shows the schematic and Supplementary Section 1 provides more details). To measure the linear transmission spectra, a collimated broadband light was linearly polarized and then weakly focused on the sample. The transmitted signal was collected on the other side of the sample by an identical lens and redirected to a spectrometer. For the nonlinear measurements, an optical parametric amplifier was used to generate a tunable pulsed laser (pulse duration, $\tau = 2\ ps$; repetition rate, $f = 80\ MHz$). The linewidth of the laser in the spectral region of interest (1,400–1,600 nm) was ~2–3 nm. The polarization and power of the laser were controlled by cascading a half-wave plate and a linear polarizer, with the linear polarizer oriented along the direction of the grating wires (Fig. 1b, y direction). By using the same lens system as in the linear measurements, the laser beam was weakly focused on the centre of the metasurface under test and then recollimated and redirected either to a photodiode or to a spectrometer (to check the spectral content of the laser) or to a near-infrared camera (for alignment purposes). The spot radius w_0 (defined as the distance from the centre at which the intensity drops by a factor e^2) on the metasurface plane was measured in each measurement run, with typical values lying within $w_0 \approx 80$–90 μm.

Two identical photodiodes (Fig. 2b, P1 and P2) were used to measure the transmission level through the metasurface. A beamsplitter was used to redirect approximately 10% of the laser power to photodiode P2 for reference. To acquire the power-dependent transmission curves (Figs. 3–5), the half-wave plate (Fig. 2b) was mounted on a motorized rotation stage. A custom-built software was used to slowly vary the impinging power by rotating the HWP and simultaneously record the signal measured by the two photodiodes. In each measurement run, the impinging power was increased up to the maximum value displayed in each plot in Figs. 3–5 and then decreased, without interruption. The sample was then flipped, and the procedure was repeated to measure the power-dependent transmission along the opposite direction. Supplementary Section 1 discusses additional details on the formulas used to calculate the average and peak intensities.

Author contributions

All authors conceived the idea and the corresponding experiment. M.C., A.C. and D.L.S. designed the device and performed the numerical analysis. M.C. fabricated the devices and performed the experimental measurements with assistance from A.C. All authors analysed the data and contributed to writing the manuscript. A.A. and A.P. supervised the project.

Competing interests

The authors declare no competing interests.

Additional information

Supplementary information The online version contains supplementary material available at https://doi.org/10.1038/s41566-023-01333-7.

Correspondence and requests for materials should be addressed to Andrea Alù.

Peer review information *Nature Photonics* thanks Lin Chang, Zongfu Yu and the other, anonymous, reviewer(s) for their contribution to the peer review of this work.

Reprints and permissions information is available at www.nature.com/reprints.